Article:

Luo, J, Chu, F, Ni, Z et al. (2 more authors) (2021) Dynamics of droplet impacting on a cone. Physics of Fluids, 33 (11). 112116. ISSN 1070-6631

https://doi.org/10.1063/5.0073049

Dynamics of droplet impacting on a cone

Jia Luo (罗佳),[1] Fuqiang Chu (褚福强),[2,a)] Zhongyuan Ni (倪中原),[1] Jun Zhang (张俊),[1,a)] and Dongsheng Wen (文东升)[1,3]

AFFILIATIONS

[1]School of Aeronautic Science and Engineering, Beihang University, Beijing 100191, China
[2]School of Energy and Environmental Engineering, University of Science and Technology Beijing, Beijing 100083, China
[3]School of Chemical and Process Engineering, University of Leeds, Leeds LS2 9JT, UK
[a)]Author to whom correspondence should be addressed: chu_fuqiang@126.com, jun.zhang@buaa.edu.cn

ABSTRACT

Droplet rebound dynamics on superhydrophobic surfaces has attracted much attention due to its importance in numerous technical applications, such as anti-icing and fluid transportation. It has been demonstrated that changing the macro-structure of the superhydrophobic surface could result in significant change in droplet morphology and hydrodynamics. Here we conduct both experimental and numerical studies of droplet impacting on a cone, and identify three different dynamic phases by changing the impacting conditions, i.e., the Weber number and the cone angle. The spreading and retracting dynamics are studied for each phase. Particularly, it is found that in Phase 3, where the droplet leaves the surface as a ring, the contact time is reduced by 54% compared with that of a flat surface. A theoretical model based on energy analysis is developed to get the rebound point in Phase 3, which agrees well with the simulation result. Besides, the effect of Weber number and cone angle on the contact time is explored. Finally, the phase diagram of the three phases distribution with We and cone angle is given, which can provide guidance to related applications.

I. INTRODUCTION

Droplet impacting onto solid surfaces is a unique phenomenon either in nature, e.g., rain falls, or in engineering fields such as anti-icing, and it has attracted great attention for many years.[1-5] Depending on the surface properties, droplet impact may present different outcomes: deposition, splashing, and rebound.[6-10] Rebound happens when droplet impacts on superhydrophobic surfaces, on which droplet will go through spreading, retracting, and rebounding due to the small liquid-solid contact area and weak adhesion of the surface.[11-17] The duration of this whole process is defined as the contact time, which is important in droplet impacting dynamics and it has been proposed that contact time scales as the inertial-capillary time τ_0 ($\tau_0 = \sqrt{\rho r_0^3/\sigma}$, where ρ is the liquid density, r_0 is the droplet initial radius, and σ is the liquid surface tension), which is independent of impact velocity (v_0).[18]

In many engineering applications, it is beneficial to reduce contact time to increase the performance of self-cleaning, anti-icing, or anti-frosting. Conventional methods to reduce contact time is to reduce liquid-solid interaction and change the surface wettability. For instance, Li et al. found that the contact time is subjected to the solid fraction of liquid contacted.[19] However, it was also proposed that, even if no liquid-solid adhesion on the surface and no liquid penetration into the surface asperities exist, there is still a theoretical contact time limit of $2.2\tau_0$ due to the symmetry in the process of spread and retraction on flat superhydrophobic surfaces.[20] Thus, approaches to break the symmetric dynamics of droplet have been carried out. Bird et al. added a macro ridge, whose height is slightly less than the spreading film thickness, to the flat superhydrophobic surfaces. It was found that liquid possessed a faster retraction along the ridge than that on the flat surface, leading to a 37% reduction in contact time.[21] Following this work, studies focused on contact time reduction by asymmetric dynamics have been carried out, including the inclined surface,[22, 23] curved surface,[24-30] surfaces with macro structures of different geometries,[31-40] moving surfaces,[41, 42] and off-center impact.[43, 44]

Besides the aforementioned asymmetric approaches, symmetric bouncing by involving the droplet center to retraction with point-like structure to reduce contact time has also been proposed. Liu et al. fabricated convex surfaces with a height of 0.6 mm and a radius of 2.0 mm and found that such structures can reduce the contact time by 28.5%.[45] A point-like structure was applied to reduce contact time by Chantelot et al., and it was proposed that droplets can lift up as a ring and a reduction in contact time can be achieved.[46]

Based on the widely existence of sharp-edged structures, there is a strong need to investigate the symmetric droplet impact behavior on point-like structures, a field that has seldom studied. The effect of impact conditions on the droplet dynamic behavior and contact time still remains unclear. To improve our understanding, we conducted a systematic investigation of droplet impacting on superhydrophobic cone surfaces with focuses on the morphologic evolution and contact time. We reveal three different phases of morphologic evolution and investigate their impacting dynamics respectively, among which a theoretical model to predict the rebound point in Phase 3 is established on the basis of energy analysis. Furthermore, the effects of Weber number and cone angle on the contact time are studied and a phase diagram delimiting three phases for impacting dynamics is proposed. We expect that this work could deepen the understanding on the droplet impacting dynamics on pointy structures and provide fundamental supports to related engineering applications such as anti-icing of the aero-engine rotating cone.

II. METHOD

A. Experimental Setup

The experimental system is shown in Fig. 1. During experiments, the droplet is produced by a syringe pump and an injector with a certain diameter determined by the needle size. The droplet falls under gravity and impacts on the cone tip with no offset distance. A high-speed camera (PCO. Dimax HS4, Germany) is applied to capture the droplet impact process and a strong light source is placed opposite the camera to achieve high-contrast image capture. The droplet diameter is measured from the images processed by Matlab and ImageJ; the impact velocity is calculated by the formula $v_0 = \sqrt{2gh}$, where g and h denote gravity acceleration and the height of the needle above cone tip, respectively. The cone is made of copper and is machined with an angle of φ. The whole surface is coated with a superhydrophobic coating fabricated by the chemical deposition-etching method.[47] As the SEM image in Fig. 1 shows, the cone surface is covered by moss-like structures. Measured by the equipment (Biolin Theta Lite, Finland), the static, advancing, and receding contact angles are 160±1.3°, 164±2.3°, and 156±2.9°, respectively, indicating excellent superhydrophobicity of the cone surface. In this work, the experiment is mainly used to validate our numerical method, which is introduced below.

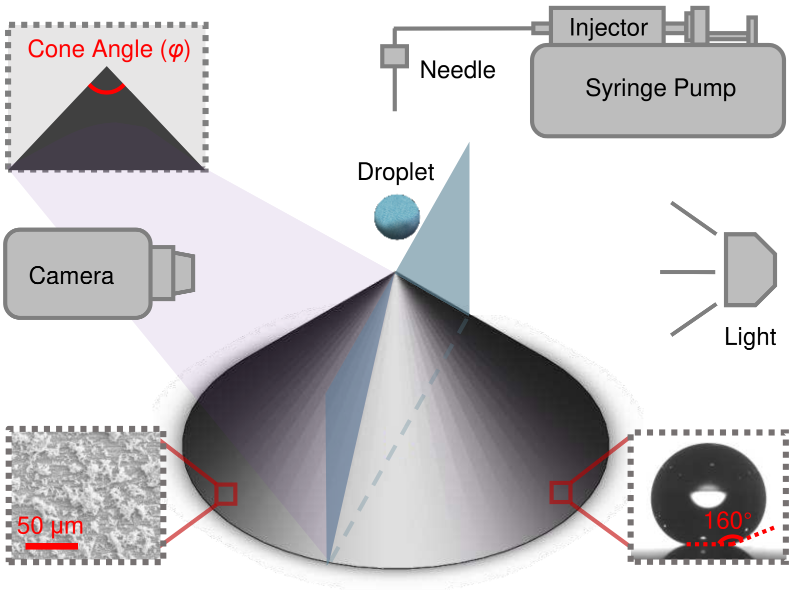

FIG. 1. Schematic of the experimental setup. The experimental system includes a droplet production module (syringe pump, injector, and needle) and a high-speed camera module (high-speed camera, light source, and computer). The cone has an angle of φ and the cone surface is superhydrophobic with moss-like structures.

B. Numerical Method

In the present work, Volume of Fluid (VOF) method is used to capture the interface of two phases, which has been successfully applied in many previous studies. In this method, the volume fraction (α) is defined to delimit different phases: $\alpha = 0$ represents that the cell is occupied by gas, $\alpha = 1$ represents that the cell is occupied by the liquid phase, and $0 < \alpha < 1$ corresponds to the interface between the two phases. The corresponding mass and momentum conservation equations are as

$$\frac{\partial \rho}{\partial t} + \nabla \cdot (\rho \boldsymbol{U}) = 0, \tag{1}$$

$$\frac{\partial \rho \boldsymbol{U}}{\partial t} + \nabla \cdot (\rho \boldsymbol{U} \boldsymbol{U}) = \nabla \cdot (\mu (\nabla \boldsymbol{U} + \nabla \boldsymbol{U}^T)) - \nabla p + \rho g + \boldsymbol{F}, \tag{2}$$

where $\boldsymbol{U}$ is the velocity vector, t is the time step, p is the pressure, and $\boldsymbol{F}$ is the volumetric surface tension force on the fluid at the gas-liquid interface, calculated by the continuum surface force (CSF) model, which is

$$\boldsymbol{F} = \sigma \kappa \nabla \alpha, \tag{3}$$

in which σ is the surface tension coefficient and κ is the mean curvature of the free surface,

$$\kappa = -\nabla \cdot \left(\frac{\nabla \alpha}{|\nabla \alpha|}\right). \tag{4}$$

In Eqs. (1) and (2), ρ and μ are calculated by the volume fraction:

$$\rho = \alpha \rho_{\text{liquid}} + (1-\alpha)\rho_{\text{gas}}, \tag{5}$$

$$\mu = \alpha \mu_{\text{liquid}} + (1-\alpha)\mu_{\text{gas}}. \tag{6}$$

The advection equation for α is employed as

$$\frac{\partial \alpha}{\partial t} + \nabla \cdot (\alpha \boldsymbol{U}) = 0. \tag{7}$$

In the present work, the dynamic contact angle model proposed by Kistler is utilized to relate the contact velocity and dynamic contact angle on the triple line, which has been validated in numerous researches.[48-50] During the simulation, the value of advancing contact angle and receding contact angle are set according to the wettability of the experimental surface.

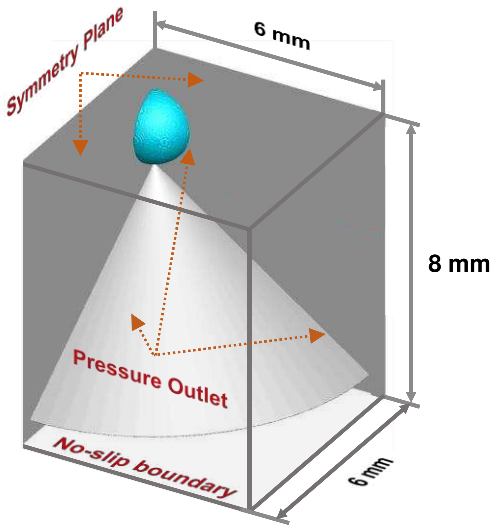

FIG. 2. Simulation setup. The computation domain is set as $6\times6\times8$ mm^3 with two adjacent surfaces as symmetry plane, the bottom surface as no-slip boundary, and the other three surfaces as pressure outlet boundaries.

In this work, the interFoam solver within the framework of Open Source Field Operation and Manipulation (OpenFOAM) is used to perform numerical simulations. The accuracy and efficiency of the interFoam solver for the simulation of multiphase flows was evaluated approvingly by Deshpande et al.,[51] and has been widely applied to the study of droplet dynamics.[52-54] Due to the rotational symmetry of the simulation, only a quarter of the computation domain of $6\times6\times8$ mm^3 is simulated to save computation resources as in Fig. 2. The bottom surface is set as the no-slip boundary with the static contact angle being 160°, two adjacent surfaces are symmetry planes, and the other surfaces are pressure outlet boundaries. Here the physical properties of the water and air at 20 ℃ are chosen. The mesh independence test is conducted with four different grids of minimum sizes of $50\times50\times50$ μm^3, $25\times25\times25$ μm^3, $12\times12\times12$ μm^3, and $6\times6\times6$ μm^3, and it shows that the result of $12\times12\times12$ μm^3 is almost the same as that of $6\times6\times6$ μm^3, so the mesh of $12\times12\times12$ μm^3 is chosen to perform the numerical work.

C. Model Validation

To support the reliability of the numerical model, the morphology comparison between experiments conducted with the devices shown in Fig. 1 and simulations set as Fig. 2 is conducted. Two series of conditions are validated to ensure the validity of the numerical model. One condition is set as a droplet impacts the flat superhydrophobic surface (the static contact angle of the surface θ is 160°, droplet radius r_0 is 1.05 mm, and the impact velocity v_0 is 0.816 m/s), and another condition is that the droplet impacts a cone with a cone angle (φ) of 50° (θ =160°, r_0 = 1.115 mm, and v_0 = 1 m/s) as shown in Fig. 3 (b) (multimedia view). The results are shown in Fig. 3 and we can see that in both conditions, the temporal evolution of morphology obtained by experiment and simulation are in good agreement, which indicates the applicability of the numerical model to predict the droplet impact phenomenon.

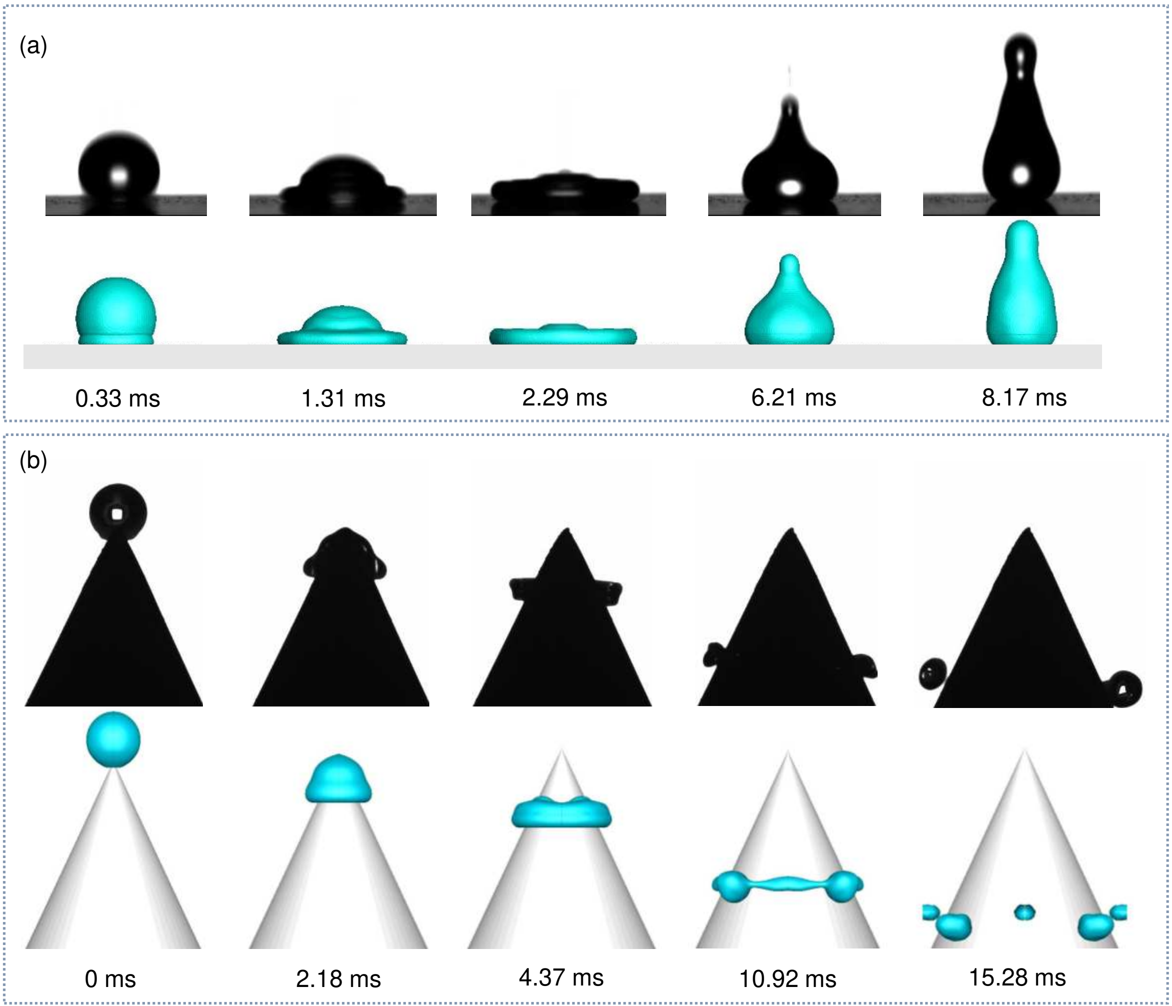

FIG. 3. Comparison between experimental results and numerical results: (a) droplet impacting on flat superhydrophobic surfaces under the condition of r_0 = 1.05 mm, v_0 = 0.816 m/s; (b) droplet impacting on a cone with an angle of 50° under condition of r_0 = 1.115 mm, v_0 =1 m/s. Both results indicate that the numerical model can well predict droplet impact behaviors (multimedia view).

III. RESULTS AND DISCUSSION

A. Morphologic Evolution and Impact Dynamics

1. Morphologic evolution

Droplet morphology is affected by the interaction between liquid and solid. Here, we classify the droplet morphology evolutions into three phases by changing the impacting velocity (v_0) and cone angle (φ). Figure. 4 (multimedia view) shows the droplet morphologic evolutions with time when the droplets impact on the cone of φ = 110°, where Phase 1, 2, and 3 are depicted in Figs. 4 (a), (b), and (c), respectively. In Phase 1 and Phase 2, droplets both rebound from the tip of the cone after impacting; differently, the droplet in Phase 2 has been impaled by the cone (top view at τ = 5.5 ms in Fig. 4 (b)), while the droplet in Phase 1 has not been impaled but rebounds immediately after reaching the maximum spreading. In Phase 3, the droplet is also impaled by the cone, but it does not rebound from the tip of the cone as in Phase 2; instead, it leaves the surface as a ring with two contact lines retracting towards each other. It should be noted that the initial position of the droplet is 0.1 mm above the cone tip at $\tau = 0.0$ ms.

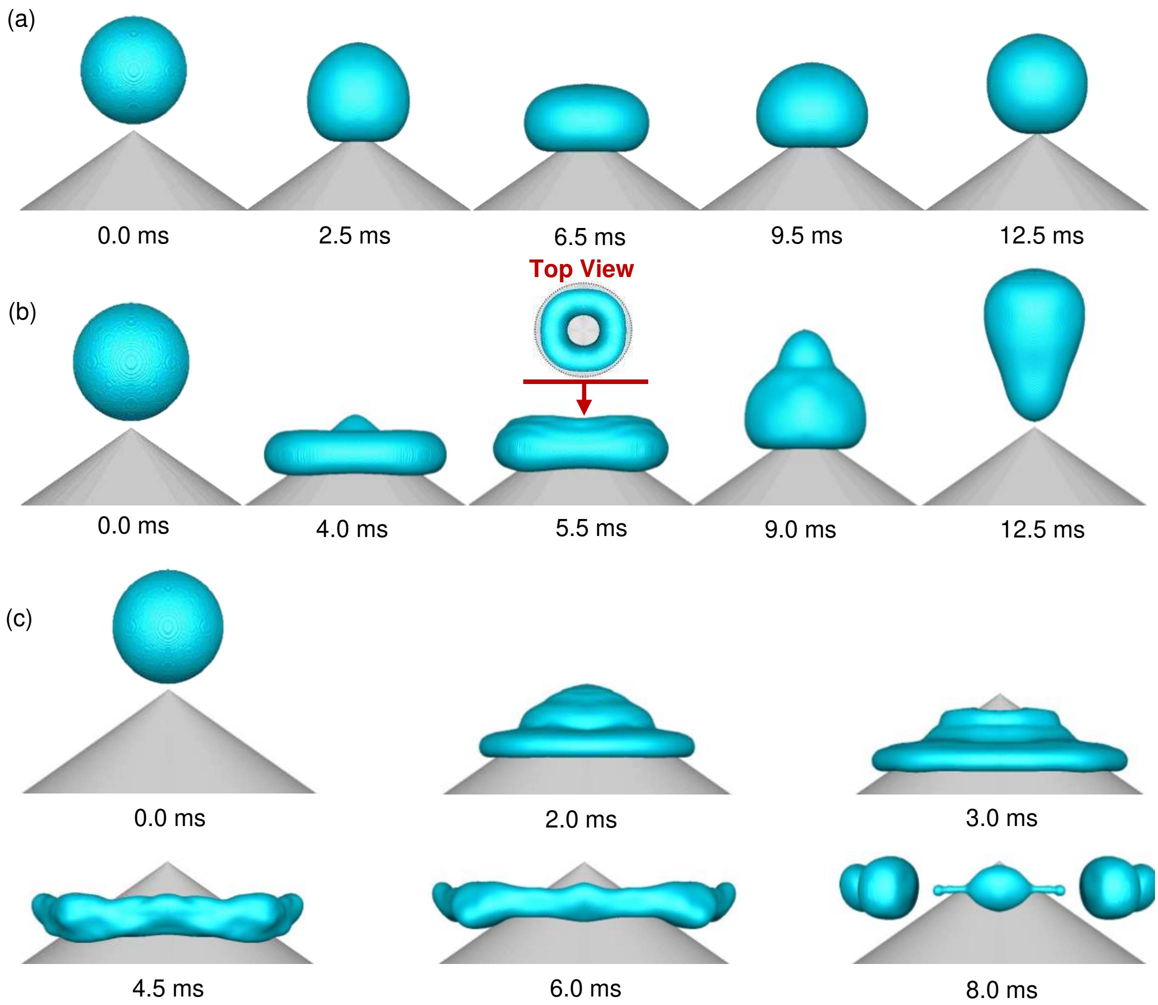

FIG. 4. Three different impact outcomes: (a) Phase 1: droplet impacts on a cone, spreads, recoils and rebounds ($r_0 = 1.0$ mm, $v_0 = 0.2$ m/s, $\varphi = 110$ °); (b) Phase 2: droplet is impaled by the cone and then rebounds from the cone tip ($r_0 = 1.0$ mm, $v_0 = 0.6$ m/s, $\varphi = 110$ °); (c) Phase 3: droplets is impaled by the cone and leaves the surface as a ring ($r_0 = 1.0$ mm, $v_0 = 1.2$ m/s, $\varphi = 110$ °). (multimedia view)

To quantitatively describe impact dynamics, variations of the pressure contour, the velocity field, and the spreading factor ($\beta = r/r_0$, where r is the spreading radius, which is defined as the parallel distance along the cone surface between the cone tip and the contact line) with time in three phases are investigated.

2. *Impact dynamics in Phase 1*

In Phase 1, the droplet firstly impacts the cone and spreads under inertial force; in this stage, the droplet goes through a deformation driven by pressure gradients ($\tau = 2.5$ ms in Fig. 5 (a)).[55] Then it reaches the maximum spreading, at which time, velocity inside the droplet is almost zero (τ = 6.5 ms in Fig. 5 (a)). Later the droplet begins to retract under capillary forces with the velocity vector upward and finally rebounds from the tip of the cone at 12.5 ms in Fig. 5 (a). Figures 5 (b) and (c) show the effect of cone angle and Weber number (We = $\rho v_0^2 d_0/\sigma$) on the spreading factor variation.

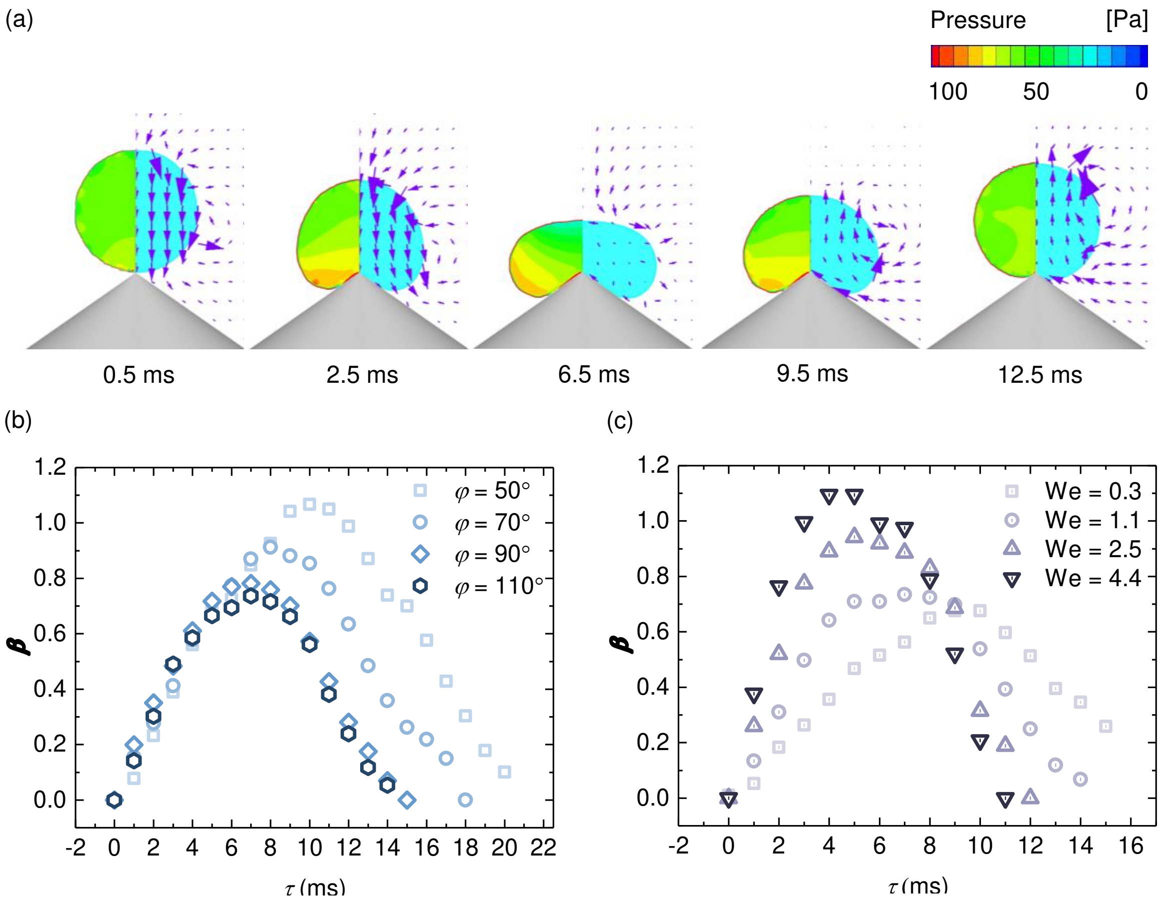

FIG. 5. Pressure distribution, velocity vector, and spreading factor in Phase 1: (a) the distribution map of pressure inside droplet (Left) and velocity vector chart inside the droplet during impact (Right) under the condition of r_0 = 1 mm, v_0 = 0.2 m/s, and φ = 110°; (b) spreading factor varying with time at different cone angles (r_0 = 1 mm, v_0 = 0.2 m/s, φ = 50°, 70°, 90°, and 110°, respectively); (c) spreading factor varying with time at different Weber numbers (φ = 110° , We = 0.3, 1.1, 2.5, and 4.4, respectively).

Droplet spreading stage is dominated by inertial force, so the spreading velocity is unrelated to cone angle (Fig. 5 (b)) and increases with impact velocity (Fig. 5 (c)). On the basis of energy analysis, during impact, the initial kinetic energy will transfer to surface energy and viscous dissipation, both of which are positively related to the liquid-solid contact area (~ $\pi r_{\max}^2\sin(\varphi/2)$). Thus, both decreasing cone angle and increasing We can increase the maximum spreading radius (Figs. 5 (b) and (c)) to guarantee the energy conservation.

As for the contact time, a shorter contact time can be reached under blunter cone angle due to the decreasing maximum spreading radius (Fig. 5 (b)). Contact time under the same cone angle decreases with increasing We, which can be explained by that, for droplet impact with low We, the deformation is small and the droplet, to some extent, could be treated as an elastic sphere, and the time scales decreases with increasing impact velocity.[56]

3. *Impact dynamics in Phase 2*

In Phase 2, firstly, the droplet impacts the cone and then spreads to the maximum contact length. However, the droplet film will be impaled because of the high pressure region and outward velocity vector at the center part of the droplet film (τ = 4.0 ms in Fig. 6 (a)). After the impalement, the droplet becomes a ring shape (τ = 5.5 ms in Fig. 6 (a)) with an internal contact line emerging. After reaching the maximum position, both the inner and outer edges start to retract and the liquid ring coalesces at the tip of the cone (τ = 9.0 ms in Fig. 6 (a)). The kinetic energy transformed from the surface energy renders the coalesced liquid an upward motion and finally lifts the droplet up from the cone tip (τ = 12.5 ms in Fig. 6 (a)).

To study the spreading and retracting dynamics in Phase 2, the effect of cone angle and We on the outer contact line spreading factor β are depicted in Figs. 6 (b) and (c), respectively. Similar to Phase 1, the spreading stage is controlled by inertial force and thus the spreading velocity of the leading edge is independent of cone angle and increases with increasing We. Besides, the maximum spreading radius increases with decreasing cone angle and increasing We (Figs. 6 (b) and (c)) as explained above.

In Phase 2, contact time increases with increasing cone angle, which is the same as it in Phase 1. When the cone angle remains unchanged, the contact time presents a similar variation with We to it on the flat superhydrophobic surfaces, which is in the scale of inertial-capillary time scale, $\sqrt{\rho r_0^3 / \sigma}$, and is independent of impact velocity, which is consistent with droplet impact on flat superhydrophobic surfaces.[18, 56-59]

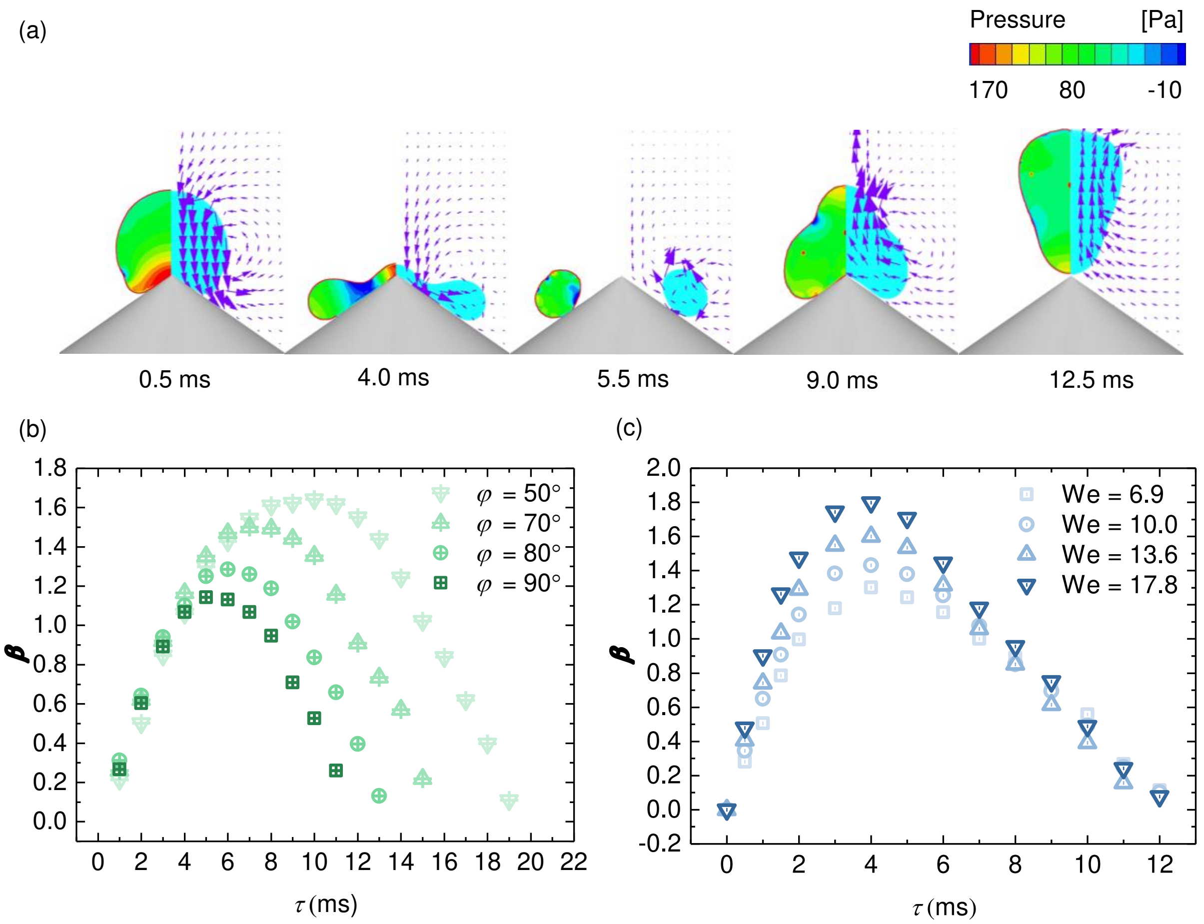

FIG. 6. Pressure distribution, velocity vector, and spreading factor in Phase 2: (a) the distribution map of pressure inside droplet (Left) and velocity vector chart inside the droplet during impact (Right) under the condition of r_0 = 1 mm, v_0 = 0.6 m/s, and φ = 110°; (b) spreading factor varying with time at different cone angle (r_0 = 1 mm, v_0 = 0.4 m/s, φ = 50°, 70°, 80°, and 90°, respectively); (c) spreading factor varying with time at different Weber number (φ = 110° , We = 6.9, 10.0, 13.6, and 17.8, respectively).

4. *Impact dynamics in Phase 3*

In Phase 3, the stages of spread and impalement are similar to those of Phase 2 (τ = 0.5~3.0 ms in Fig .7); however, different from Phase 2, the inner contact line moves towards the outer contact line (τ = 3.0 ms in Fig .7) and the two contact lines coincide with each other and the contact region between liquid and solid becomes a line (τ = 4.5 ms in Fig .7). At this moment, there is an upward velocity vector perpendicular to the surface which is similar to the retraction process on flat surfaces, and the droplet rebounds upwards finally.

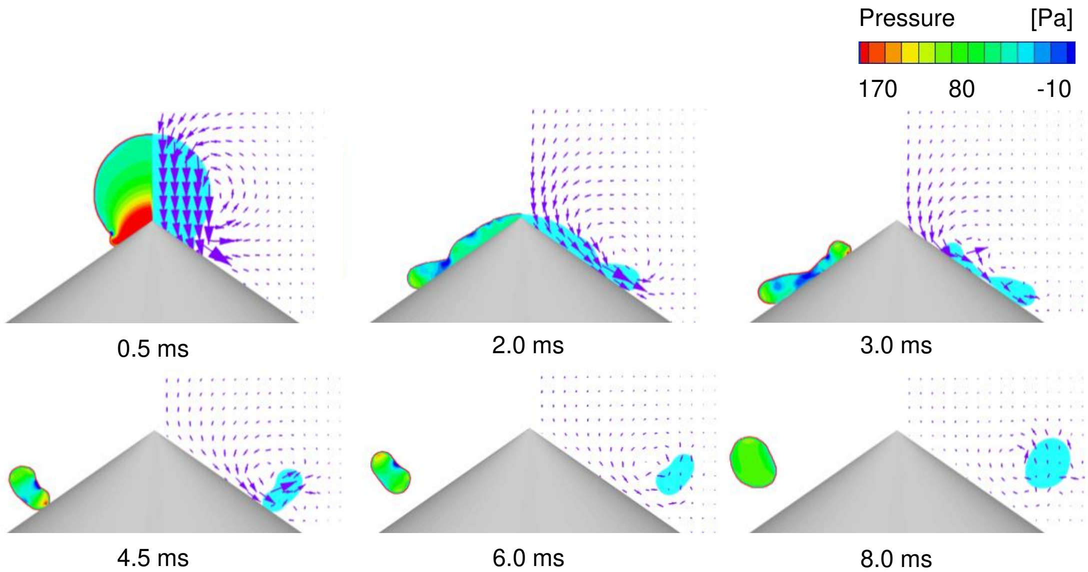

FIG. 7. Pressure distribution and velocity vector of Phase 3: the distribution map of pressure inside droplet (Left) and velocity vector chart inside the droplet during impact (Right) under the condition of r_0 = 1 mm, v_0 = 1.2 m/s, and φ = 110°.

The inner and outer contact radius variations with time are shown in Fig. 8 (a) (r_0 = 1.0 mm, v_0 = 1.2 m/s, φ = 80°), where r_{in} represents spreading radius of the inner contact line and r_{out} represents spreading radius of the outer contact line. The three insert graphs in Fig. 8 (a) are the droplet morphologies at τ = 2.0, 3.0, and 4.0 ms, respectively. During τ = 0.0 ~ 2.0 ms, the outer contact line spreads along the cone surface; and at τ = 2.0 ms, the droplet is impaled by the cone tip and the inner contact line starts to retract along the cone surface; during τ = 2.0 ~ 4.5 ms, both outer and inner contact lines move along the surface, but because the retract velocity of inner contact length is faster than the outer one for the thinner film thickness of the inner part,[60] the two contact lines collide with each other and all parts of the droplet rebound from the cone (τ = 4.5 ms). The spreading radius at the collision moment is defined as the final contact radius, r_f.

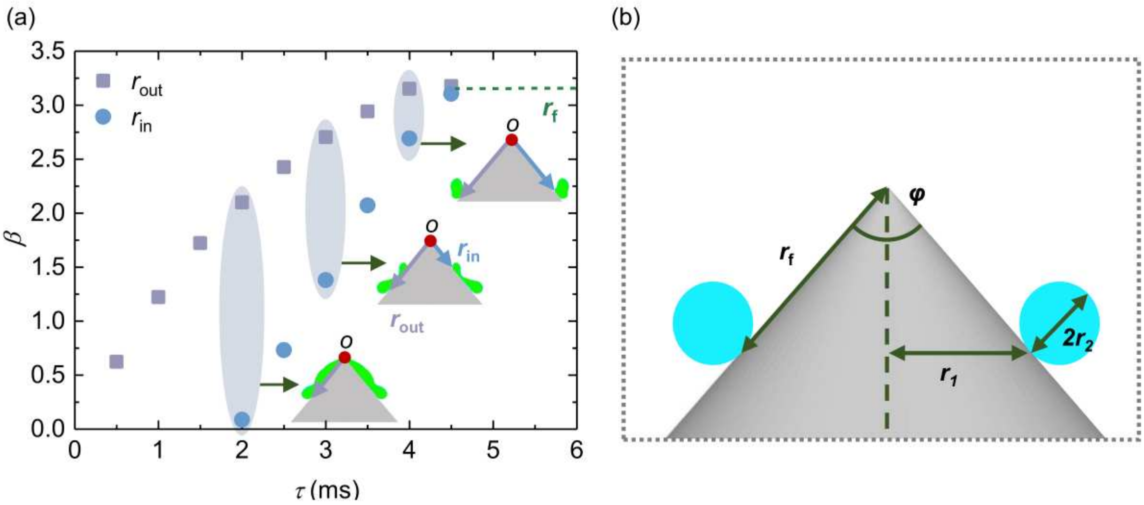

FIG. 8. (a) Spreading factor varying with time in Phase 3 (r_0 = 1.0 mm, v_0 = 1.2 m/s, φ = 80°), where square and circle dots refer to outer contact line spread radius (r_{out}) and inner line spread radius after impalement (r_{in}), respectively. r_f is the spreading radius when the two contact lines coincide, which is also the rebound moment. (b) droplet profile at the rebound moment.

The diagram of the droplet morphology at the collision moment is shown in Fig. 8 (b), which is a ring shape characterized by the two radius dimensions: r_1 and r_2; besides, the cone angle φ and the final contact radius r_f are also indicated. The value of r_f determines where the drop ring rebounds from the cone surface, so the theoretical value is deduced by energy methods. The energy involved in the droplet impact process mainly includes kinetic energy, surface energy, and viscous dissipation. Before impact, the initial kinetic energy E_{k0} and surface energy E_{s0} are

$$E_{k0} = \frac{2}{3}\pi\rho r_0^3 v_0^2, \tag{8}$$

$$E_{s0} = 4\pi\sigma r_0^2. \tag{9}$$

According to the diagram in Fig. 8 (b), the surface energy at the collision moment is

$$E_s = 4\pi^2\sigma(r_1 + r_2)r_2. \tag{10}$$

The relation between r_1 and r_2 can be obtained by the conservation of liquid volume due to the incompressibility of the liquid. And the liquid volume at initial and collision time is

$$V_0 = \frac{4}{3}\pi r_0^3, \tag{11}$$

$$V_f = 2\pi^2(r_1 + r_2)r_2^2. \tag{12}$$

By $V_0 = V_f$, the ring characteristic size r_1 can be expressed by r_2:

$$r_1 = \frac{2r_0^3}{3\pi r_2^2} - r_2. \tag{13}$$

The viscous dissipation involved can be calculated using the formula:[61]

$$W = \int_0^{\tau_f}\int_\Omega \Phi \mathrm{d}\Omega \mathrm{d}t = \Phi\Omega\tau_f. \tag{14}$$

where Φ is the viscous dissipation function and can be expressed as $\Phi = \mu(v_0/\delta)^2$ ($\delta = 2d_0/\sqrt{Re}$ is the thickness of the boundary layer) and Ω is the volume of the viscous fluid calculated by $\Omega = \pi r_1^2/\sin(\varphi/2)\delta$, and the time duration τ_f is estimated by $\tau_f = 8d_0/3v_0$.[62] Thus, the viscous dissipation in Eq. (14) can be changed to

$$W = \frac{4\pi\mu v_0 r_1^2\sqrt{\mathrm{Re}}}{3\sin(\varphi/2)}. \tag{15}$$

For the kinetic energy at the collision moment, according to our simulation results ($E_s = 5.3\times10^{-7}$, $W = 3.4\times10^{-7}$, $E_k = 3.8\times10^{-8}$, at the condition of d_0 = 2.0 mm, v_0 = 1.2 m/s, and φ = 110°), it is assumed that the residual kinetic energy is negligible to simplify the theoretical analysis,

$$E_k \approx 0\,. \tag{16}$$

During the droplet impact process, the energy conservation is expressed as

$$E_{k0} + E_{s0} = E_k + E_s + W\,. \tag{17}$$

We can obtain the relationship between the characterized size β_2 ($\beta_2 = r_2/r_0$) and the impact conditions (We and φ) by substituting energy terms of Eqs. (8), (9), (10), (15), and (16) into the conservation equation of Eq. (17):

$$\left[\frac{1}{3} - \frac{4}{3\sin(\varphi/2)\sqrt{Re}}\left(\frac{2}{3\pi\beta_2^2} - \beta_2\right)^2\right]We - \frac{8}{3\beta_2} + 4 = 0\,. \tag{18}$$

Due to Eq. (13) and $r_f = r_1/\sin(\varphi/2)$, Eq. (18) can be converted to the relationship between r_f and impact conditions (We and φ). Figure 9 compares the droplet contact length ratio $\beta_f = r_f/r_0$ at the rebound moment with different We and cone angles obtained from the simulation (scatter point) and theoretical model (line). As shown in Fig. 9, β_f presents the same increasing trend with We at different cone angles, and it decreases with increasing cone angle, which is similar to Phase 2. Both Figs. 9 (a) and (b) show the good agreement between simulation results and theoretical results and indicate the availability of the theoretical model. The discrepancy between the theoretical and numerical value can be explained by the assumption that the residual kinetic energy, E_k, equals zero, which slightly overestimates the energy for the droplet to spread on the cone and makes the theoretical value of the spreading factor larger than the numerical value.

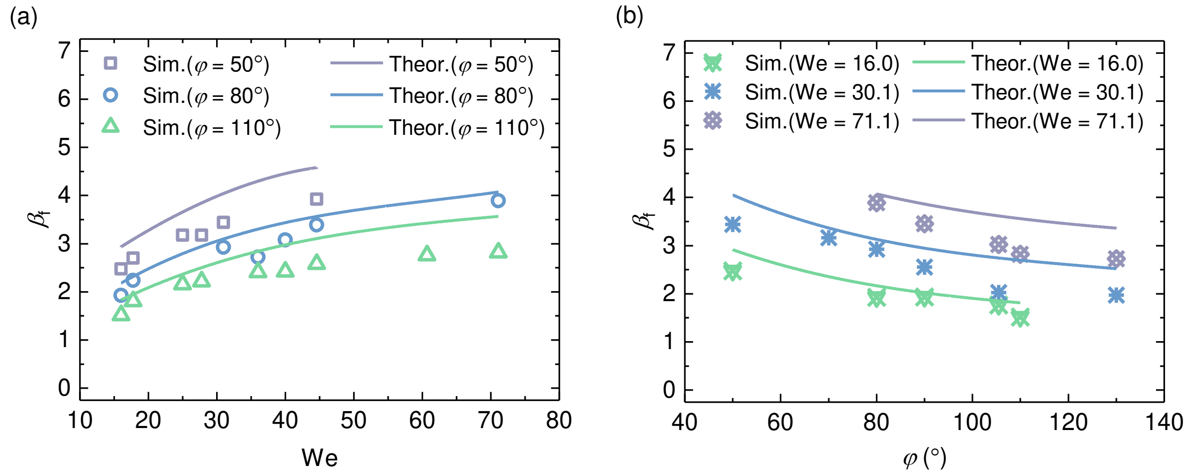

FIG. 9. Comparison between theoretical value and simulation value of spreading factor at collision moment ($\beta_f = r_f/r_0$): (a) β_f varies with Weber number (φ = 50°, 80°, and 110°); (b) β_f varies with cone angle (We = 16.0, 30.1, and 71.1).

To clearly observe the contact length variation with time in Phase 3, the effect of We and cone angle on the absolute contact length ($\beta_{out\text{-}in} = \beta_{out} - \beta_{in}$), the dimensionless expression of the absolute contact length $r_{out\text{-}in}$, is depicted in Fig. 10. In Fig. 10, the maximum value of $\beta_{out\text{-}in}$ emerges at the moment when the droplet is impaled by the cone tip, and after this moment the absolute contact length of the droplet decreases with time due to the movement of inner contact line towards the outer one; finally, the time when the value of $\beta_{out\text{-}in}$ equals zero corresponds the collision of the two contact lines and the rebound of the droplet.

The whole impact process in Phase 3 can be divided into two stages, one of which is the stage before impalement and another is the process between the impalement and the rebound moment, and the time durations of these two stages are defined as τ_{impale} and $\tau_{retract}$, respectively.

With increasing cone angle, due to the more blunt cone tip, it is more difficult to impale the liquid film and the time reaching the impalement (τ_{impale}) increases (Fig. 10 (c)); thus, the contact length at the impalement moment (r_{impale}) increases (Fig. 10 (a)) and the corresponding film thickness decreases, which causes the inner contact line posess a higher retraction velocity (v_{in}). We can conclude that droplet posseses a higher absolute shrinking velocity ($v_{out\text{-}in}$) as shown in Fig. 10 (a) and a shorter retraction time duration ($\tau_{retract}$) (Fig. 10 (c)).

With increasing We, the spreading velocity increases and it is easier to impale the liquid film with more initial kinetic energy; thus τ_{impale} decreases and r_{impale} increases (Figs. (b) and (d)). As mentioned above, v_{in} increases with increasing r_{impale}; however, at high We, the outer contact line still posseses a high kinetic energy which plays a major role, so $v_{out\text{-}in}$ presents a decreasing trend (Fig. 10 (b)) and $\tau_{retract}$ increases with increasing We (Fig. 10 (d)).

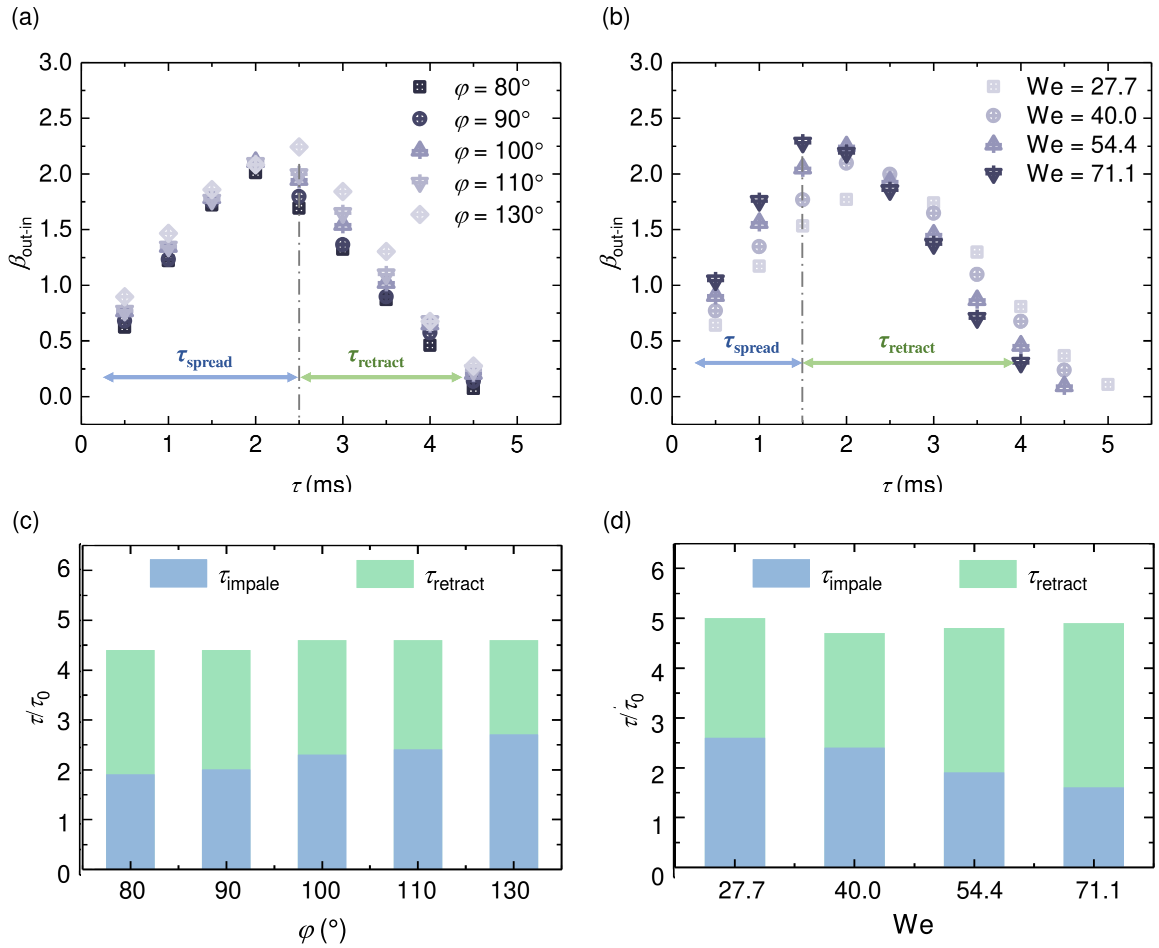

FIG. 10. Absolute contact line spreading factor ($\beta_{out\text{-}in}$) varying with time (a) under different cone angles (φ = 80°, 90°, 100°, 110°, and 130°) and (b) Weber number (We = 27.7, 40.0, 54.4, and 71.1). Variation of the time reaching the impalment moment (τ_{impale}) and the time duration for retraction ($\tau_{retract}$) (c) under different cone angles (φ = 80°, 90°, 100°, 110°, and 130°) and (d) under different Weber number (We = 27.7, 40.0, 54.4, and 71.1).

B. Contact Time and Phase Diagram

On the basis of the above analysis for the droplet hydrodynamics in different phases, in the next section, the contact time in different phases is studied, where the contact time is defined as the time duration between the moment when the droplet contacts with the cone tip and the time at which droplet leaves the surface, and it is normalized by the inertial-capillary time, $\tau_0 = (\rho r_0^3/\sigma)^{1/2}$. The effect of cone angles and We on the contact time is studied, and the diagram of different phases distribution with cone angles and We is obtained.

Figure 11 (a) shows the contact time as a function of the cone angle in different phases. For droplet impacts in Phase 1 and 2, contact time decreases with increasing cone angle, which is consistent with the impact dynamics in Fig. 5 (b) and Fig. 6 (b); and this is caused by the increasing time for reaching the maximum contact length. For droplet impacts in Phase 3, the contact time is independent of the cone angle, which can be understood by the analysis in Fig. 10 (a) that droplet possesses a longer spreading time τ_{impale} and a shorter retraction time $\tau_{retract}$. In Fig. 11 (a), it is also found that contact time in Phase 1 and Phase 2 (We = 1.1 and We = 6.9) almost coincide with each other, and this is related to the relationship between contact time and We, which will be discussed in the next section.

In Fig. 11 (b), the contact time varying with We under three different cone angles, φ =80°, 90°, and 110°, is depicted, which shows that under each cone angle, contact time presents three different trends corresponding to different phases. Firstly, in Phase 1 which is represented by purple background, contact time decreases with increasing We; in Phase 2 which is represented by green background, contact time remains almost constant with varying We; and in Phase 3 which is represented by yellow background, contact time still remains unchanged with varying We at a lower value compared with it in Phase 2. Compared with the dimensionless contact time of droplet impacting on flat surface, τ_{flat}/τ_0 =2.6, the contact time in Phase 1 and Phase 2 are longer, indicating that droplet impacting on cone in Phase 1 and Phase 2 cannot reduce droplet contact time. Conversely, droplet impacting on cone in Phase 3 can reduce the dimensionless contact time from 2.6 to 1.2, which is about 54% reduction for the retraction of both the inner and outer contact line.

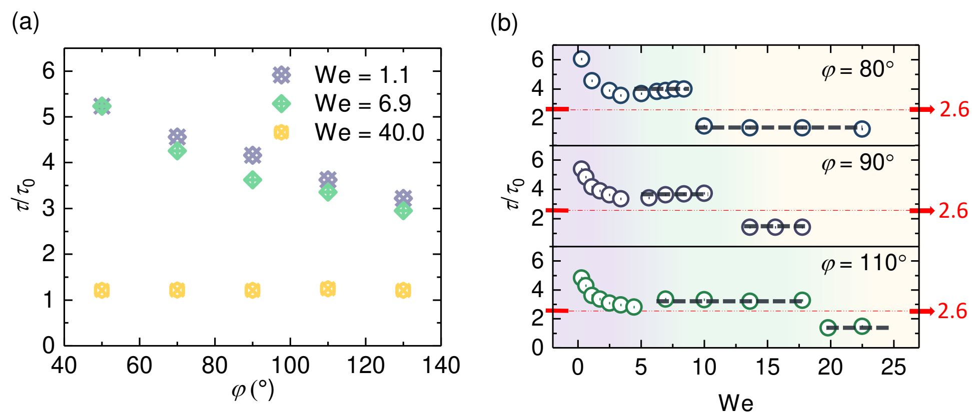

FIG. 11. The effect of impact conditions on contact time in different phases. (a) Variation of the contact time with cone angles: purple points with We = 1.1 refer to cases in Phase 1; green points with We = 6.9 refer to cases in Phase 2; and

yellow points with We = 40.0 refer to cases in Phase 3. (b) Variation of the contact time with We under different cones with φ = 80°, 90°, and 110°.

To reveal the corresponding cone angle and We for the occurrence of different impact phases, we propose a phase diagram delimiting the above three phases as in Fig. 12. It could be observed that at the low cone angle (φ = 50°), Phase 1 and Phase 2 emerge at low We, and Phase 3 happens in a wide range of We; with increasing cone angle, the range of We corresponding to Phase 2 expands while the range of Phase 1 changes less. For the boundary between Phase 1 and 2, with increasing cone angle, phases transition becomes sensitive to We; for the boundary between Phase 2 and 3, the critical We is positively correlated with the cone angle. This diagram reveals impact conditions under which different phases could occur and provides a guidance for relevant applications and requirements.

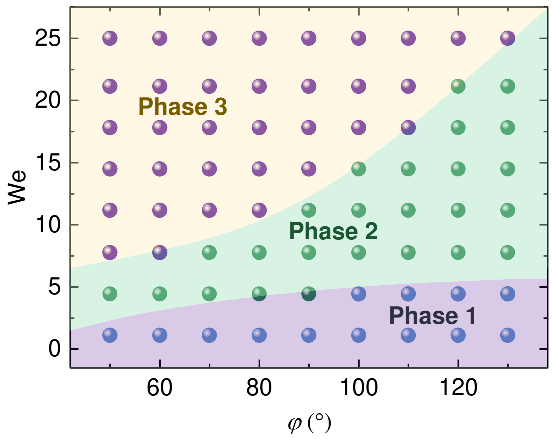

FIG. 12. Phase diagram distinguishing three phases under the conditions in this work (θ = 160°, and the fluid used here is water and air at 20 ℃): blue points represent Phase 1, green points represent Phase 2, and purple points represent Phase 3.

IV. CONCLUSIONS

In summary, we investigate the droplet impacting dynamics on superhydrophobic cones and discuss the morphologic evolution characteristics, as well as the variation of contact time. By proper selections of Weber number and cone angle, there are three typical morphologic evolution phases and each phase exhibits different impact dynamics. In Phase 1, the droplet undergoes a rebound without impalement, which is similar to that on flat surfaces; in Phase 2, the droplet is impaled by the cone, but the re-coalescence of the ring morphology lifts the droplet up from the cone tip; in Phase 3, the droplet leaves the cone surface as a ring after impalement, and a theoretical model to predict the rebound point is established, which agrees well with the numerical results. The variation of contact time exhibits different tendencies in the above phases. The contact time continuously reduces with the increase of We in Phase 1, while it remains almost constant in Phase 2, both of which are larger than that on flat surfaces. In Phase 3, a sharp reduction in contact time is observed which is about 54% compared with flat surfaces. Besides, the effect of cone angle on the contact time in different phases is studied: in Phase 1 and Phase 2, contact time decreases with increasing cone angle, while in Phase 3, contact time is independent of the cone angle. A phase diagram delimiting three phases for impacting dynamics is finally proposed, and the critical Weber number of different phases increases with increasing cone angle. The above findings pioneer in quantitatively clarifying the droplet impacting dynamics on superhydrophobic cones, which shall further guide related engineering applications.

ACKNOWLEDGEMENTS

This work was supported by the National Natural Science Foundation of China (No. 11772034) and the Integrated Projects utilizing the Space Environment on ISS and CSS supported by CMSA and ESA (No. TGMTYY00-RW-03).

DATA AVAILABILITY

The data that support the findings of this study are available within the article.

REFERENCES

[1]C. Josserand, and S. T. Thoroddsen, "Drop Impact on a Solid Surface," Annu. Rev. Fluid Mech. **48**, 365–391 (2016).
[2]L. Mishchenko, B. Hatton, V. Bahadur, J. A. Taylor, T. Krupenkin, and J. Aizenberg, "Design of Ice-free Nanostructured Surfaces Based on Repulsion of Impacting Water Droplets," Acs Nano **4**, 7699-7707 (2010).
[3]X. K. Wang, J. Zeng, X. Q. Yu, and Y. F. Zhang, "Superamphiphobic coatings with polymer-wrapped particles: enhancing water harvesting," J. Mater. Chem. A **7**, 5426-5433 (2019).
[4]W. H. Xu, H. X. Zheng, Y. Liu, X. F. Zhou, C. Zhang, Y. X. Song, X. Deng, M. Leung, Z. B. Yang, R. X. Xu, Z. L. Wang, X. C. Zeng, and Z. K. Wang, "A droplet-based electricity generator with high instantaneous power density," Nature **578**, 392-396 (2020).
[5]J. H. Kim, "Spray cooling heat transfer: The state of the art," Int. J. Heat Fluid Flow **28**, 753-767 (2007).
[6]C. L. Tang, M. X. Qin, X. Y. Weng, X. H. Zhang, P. Zhang, J. L. Li, and Z. H. Huang, "Dynamics of droplet impact on solid surface with different roughness," Int. J. Multiph. Flow **96**, 56-69 (2017).
[7]I. V. Roisman, A. Lembach, and C. Tropea, "Drop splashing induced by target roughness and porosity: The size plays no role," Adv. Colloid Interface Sci. **222**, 615-621 (2015).
[8]S. J. Lin, B. Y. Zhao, S. Zou, J. W. Guo, Z. Wei, and L. Q. Chen, "Impact of viscous droplets on different wettable surfaces: Impact phenomena, the maximum spreading factor, spreading time and post-impact oscillation," J. Colloid Interface Sci. **516**, 86-97 (2018).
[9]D. Khojasteh, M. Kazerooni, S. Salarian, and R. Kamali, "Droplet impact on superhydrophobic surfaces: A review of recent developments," J. Ind. Eng. Chem. **42**, 1-14 (2016).
[10]C. Antonini, A. Amirfazli, and M. Marengo, "Drop impact and wettability: From hydrophilic to superhydrophobic surfaces," Phys. Fluids **24**, 13 (2012).
[11]M. Y. Cao, D. W. Guo, C. M. Yu, K. Li, M. J. Liu, and L. Jiang, "Water-Repellent Properties of Superhydrophobic and Lubricant-Infused "Slippery" Surfaces: A Brief Study on the Functions and

Applications," ACS Appl. Mater. Interfaces **8**, 3615-3623 (2016).

[12]Y. Y. Wang, J. Xue, Q. J. Wang, Q. M. Chen, and J. F. Ding, "Verification of Icephobic/Anti-icing Properties of a Superhydrophobic Surface," ACS Appl. Mater. Interfaces **5**, 3370-3381 (2013).

[13]T. Maitra, C. Antonini, M. K. Tiwari, A. Mularczyk, Z. Imeri, P. Schoch, and D. Poulikakos, "Supercooled Water Drops Impacting Superhydrophobic Textures," Langmuir **30**, 10855-10861 (2014).

[14]Y. Yamauchi, M. Tenjimbayashi, S. Samitsu, and M. Naito, "Durable and Flexible Superhydrophobic Materials: Abrasion/Scratching/Slicing/Droplet Impacting/Bending/Twisting-Tolerant Composite with Porcupinefish-Like Structure," ACS Appl. Mater. Interfaces **11**, 32381-32389 (2019).

[15]C. J. Lv, P. F. Hao, X. W. Zhang, and F. He, "Drop impact upon superhydrophobic surfaces with regular and hierarchical roughness," Appl. Phys. Lett. **108**, 141602 (2016).

[16]D. Richard, and D. Quere, "Bouncing water drops," Europhys. Lett. **50**, 769-775 (2000).

[17]J. de Ruiter, R. Lagraauw, D. van den Ende, and F. Mugele, "Wettability-independent bouncing on flat surfaces mediated by thin air films," Nat. Phys. **11**, 48-53 (2015).

[18]D. Richard, C. Clanet, and D. Quere, "Surface phenomena - Contact time of a bouncing drop," Nature **417**, 811 (2002).

[19]X. Li, X. Ma, and Z. Lan, "Dynamic Behavior of the Water Droplet Impact on a Textured Hydrophobic/Superhydrophobic Surface: The Effect of the Remaining Liquid Film Arising on the Pillars' Tops on the Contact Time," Langmuir **26**, 4831-4838 (2010).

[20]J. W. Strutt, "VI. On the capillary phenomena of jets," Proc. R. Soc. Lond. **29**, 71-97 (1879).

[21]J. C. Bird, R. Dhiman, H. M. Kwon, and K. K. Varanasi, "Reducing the contact time of a bouncing drop," Nature **503**, 385-388 (2013).

[22]D. G. K. Aboud, and A. M. Kietzig, "On the Oblique Impact Dynamics of Drops on Superhydrophobic Surfaces. Part II: Restitution Coefficient and Contact Time," Langmuir **34**, 9889-9896 (2018).

[23]H. Wang, C. Liu, H. Y. Zhan, and Y. H. Liu, "Droplet Asymmetric Bouncing on Inclined Superhydrophobic Surfaces," Acs Omega **4**, 12238-12243 (2019).

[24]Y. H. Liu, M. Andrew, J. Li, J. M. Yeomans, and Z. K. Wang, "Symmetry breaking in drop bouncing on curved surfaces," Nat. Commun. **6**, 10034 (2015).

[25]M. Abolghasemibizaki, R. L. McMasters, and R. Mohammadi, "Towards the shortest possible contact time: Droplet impact on cylindrical superhydrophobic surfaces structured with macro-scale features," J. Colloid Interface Sci. **521**, 17-23 (2018).

[26]J. Q. Hou, J. Y. Gong, X. Wu, Q. W. Huang, and Y. Li, "Fast droplet bouncing induced by asymmetric spreading on concave superhydrophobic surfaces," Colloids Surf. A Physicochem. Eng. Asp. **622**, 126588 (2021).

[27]J. Luo, S.-Y. Wu, L. Xiao, and Z.-L. Chen, "Parametric influencing mechanism and control of contact time for droplets impacting on the solid surfaces," Int. J. Mech. Sci. **197**, 106333 (2021).

[28]X. Liu, X. Zhang, and J. C. Min, "Maximum spreading of droplets impacting spherical surfaces," Phys. Fluids **31**, 092109 (2019).

[29]X. Liu, J. Min, and X. Zhang, "Dynamic behavior and maximum spreading of droplets impacting concave spheres," Phys. Fluids **32**, 092109 (2020).

[30]H. N. Dalgamoni, and X. Yong, "Numerical and theoretical modeling of droplet impact on spherical surfaces," Phys. Fluids **33**, 052112 (2021).

[31]D. J. Lin, L. Z. Zhang, M. C. Yi, S. R. Gao, Y. R. Yang, and X. D. Wang, "Contact time on inclined superhydrophobic surfaces decorated with parallel macro -ridges," Colloids Surf. A Physicochem. Eng. Asp. **599**, 124924 (2020).

[32]D. J. Lin, L. Wang, X. D. Wang, and W. M. Yan, "Reduction in the contact time of impacting droplets by decorating a rectangular ridge on superhydrophobic surfaces," Int. J. Heat Mass Transf. **132**, 1105-1115 (2019).
[33]K. Regulagadda, S. Bakshi, and S. K. Das, "Triggering of flow asymmetry by anisotropic deflection of lamella during the impact of a drop onto superhydrophobic surfaces," Phys. Fluids **30**, 072105 (2018).
[34]Z. F. Hu, X. Zhang, S. H. Gao, Z. P. Yuan, Y. K. Lin, F. Q. Chu, and X. M. Wu, "Axial spreading of droplet impact on ridged superhydrophobic surfaces," J. Colloid Interface Sci. **599**, 130-139 (2021).
[35]H. Y. Liu, F. Q. Chu, J. Zhang, and D. S. Wen, "Nanodroplets impact on surfaces decorated with ridges," Phys. Rev. Fluids **5**, 15 (2020).
[36]S. Yun, "Ellipsoidal drop impact on a single-ridge superhydrophobic surface," Int. J. Mech. Sci. **208**, 106677 (2021).
[37]Y. J. Xu, L. L. Tian, C. L. Zhu, and N. Zhao, "Reduction in the contact time of droplet impact on superhydrophobic surface with protrusions," Phys. Fluids **33**, 073306 (2021).
[38]C. B. Liu, Q. Liu, and Z. H. Lin, "Dynamical behavior of droplets transiently impacting on superhydrophobic microstructures," Phys. Fluids **32**, 103304 (2020).
[39]M. Baggio, and B. Weigand, "Numerical simulation of a drop impact on a superhydrophobic surface with a wire," Phys. Fluids **31**, 112107 (2019).
[40]S. Y. Ding, Z. F. Hu, L. Y. Dai, X. Zhang, and X. M. Wu, "Droplet impact dynamics on single-pillar superhydrophobic surfaces," Phys. Fluids **33**, 102108 (2021).
[41]X. Zhang, Z. Zhu, C. Zhang, and C. Yang, "Reduced contact time of a droplet impacting on a moving superhydrophobic surface," Appl. Phys. Lett. **117**, 151602 (2020).
[42]H. Y. Zhan, C. G. Lu, C. Liu, Z. A. K. Wang, C. J. Lv, and Y. H. Liu, "Horizontal Motion of a Superhydrophobic Substrate Affects the Drop Bouncing Dynamics," Phys. Rev. Lett. **126**, 5 (2021).
[43]K. Regulagadda, S. Bakshi, and S. K. Das, "Morphology of drop impact on a superhydrophobic surface with macro-structures," Phys. Fluids **29**, 082104 (2017).
[44]Z. F. Hu, X. M. Wu, F. Q. Chu, X. Zhang, and Z. P. Yuan, "Off-centered droplet impact on single-ridge superhydrophobic surfaces," Exp. Therm. Fluid Sci. **120**, 110245 (2021).
[45]Y. Z. Shen, S. Y. Liu, C. L. Zhu, J. Tao, Z. Chen, H. J. Tao, L. Pan, G. Y. Wang, and T. Wang, "Bouncing dynamics of impact droplets on the convex superhydrophobic surfaces," Appl. Phys. Lett. **110**, 221601 (2017).
[46]P. Chantelot, A. M. Moqaddam, A. Gauthier, S. S. Chikatamarla, C. Clanet, I. V. Karlin, and D. Quere, "Water ring-bouncing on repellent singularities," Soft matter **14**, 2227-2233 (2018).
[47]F. Q. Chu, and X. M. Wu, "Fabrication and condensation characteristics of metallic superhydrophobic surface with hierarchical micro-nano structures," Appl. Surf. Sci. **371**, 322-328 (2016).
[48]S. K. Li, F. Q. Chu, J. Zhang, D. Brutin, and D. S. Wen, "Droplet jumping induced by coalescence of a moving droplet and a static one: Effect of initial velocity," Chem. Eng. Sci. **211**, 115252 (2020).
[49]A. A. Saha, and S. K. Mitra, "Effect of dynamic contact angle in a volume of fluid (VOF) model for a microfluidic capillary flow," J. Colloid Interface Sci. **339**, 461-480 (2009).
[50]S. Ding, X. Liu, X. Wu, and X. Zhang, "Droplet breakup and rebound during impact on small cylindrical superhydrophobic targets," Phys. Fluids **32**, 102106 (2020).
[51]S. S. Deshpande, L. Anumolu, and M. F. Trujillo, "Evaluating the performance of the two-phase flow solver interFoam," Comput. Sci. Discov. **5**, 014016 (2012).
[52]J. Zhang, M. K. Borg, and J. M. Reese, "Multiscale simulation of dynamic wetting," Int. J. Heat Mass Transf. **115**, 886-896 (2017).
[53]A. M. P. Boelens, A. Latka, and J. J. de Pablo, "Observation of the pressure effect in simulations of droplets splashing on a dry surface," Phys. Rev. Fluids **3**, 063602 (2018).

[54]H. Y. Liu, J. Zhang, P. Capobianchi, M. K. Borg, Y. H. Zhang, and D. S. Wen, "A multiscale volume of fluid method with self-consistent boundary conditions derived from molecular dynamics," Phys. Fluids **33**, 062004 (2021).

[55]J. Eggers, M. A. Fontelos, C. Josserand, and S. Zaleski, "Drop dynamics after impact on a solid wall: Theory and simulations," Phys. Fluids **22**, 062101 (2010).

[56]K. Okumura, F. Chevy, D. Richard, D. Quere, and C. Clanet, "Water spring: A model for bouncing drops," Europhys. Lett. **62**, 237-243 (2003).

[57]M. Reyssat, A. Pepin, F. Marty, Y. Chen, and D. Quere, "Bouncing transitions on microtextured materials," Europhys. Lett. **74**, 306-312 (2006).

[58]D. Bartolo, F. Bouamrirene, E. Verneuil, A. Buguin, P. Silberzan, and S. Moulinet, "Bouncing or sticky droplets: Impalement transitions on superhydrophobic micropatterned surfaces," Europhys. Lett. **74**, 299-305 (2006).

[59]C. Clanet, C. Beguin, D. Richard, and D. Quere, "Maximal deformation of an impacting drop," J. Fluid Mech. **517**, 199-208 (2004).

[60]D. Bartolo, C. Josserand, and D. Bonn, "Retraction dynamics of aqueous drops upon impact on non-wetting surfaces," J. Fluid Mech. **545**, 329-338 (2005).

[61]S. Chandra, and C. T. Avedisian, "On the collision of a droplet with a solid surface," Proc. R. Soc. Lond.. Series A: Mathematical and Physical Sciences **432**, 13-41 (1991).

[62]M. Pasandideh-Fard, Y. M. Qiao, S. Chandra, and J. Mostaghimi, "Capillary effects during droplet impact on a solid surface," Phys. Fluids **8**, 650-659 (1996).